Research Article Vol. 28, No. 5 / 2 March 2020 / Optics Express 7691
Optics EXPRESS

Modelling Fabry-Pérot etalons illuminated by focussed beams

DYLAN M. MARQUES,* JAMES A. GUGGENHEIM, REHMAN ANSARI, EDWARD Z. ZHANG, PAUL C. BEARD, AND PETER R. T. MUNRO

Department of Medical Physics and Biomedical Engineering, University College London, London, UK
dylan.marques.17@ucl.ac.uk

Abstract: Fabry-Pérot (FP) etalons are used as filters and sensors in a range of optical systems. Often FP etalons are illuminated by collimated laser beams, in which case the transmitted and reflected light fields can be calculated analytically using well established models. However, FP etalons are sometimes illuminated by more complex beams such as focussed Gaussian beams, which may also be aberrated. Modelling the response of FP etalons to these beams requires a more sophisticated model. To address this need, we present a model that can describe the response of an FP etalon that is illuminated by an arbitrary beam. The model uses an electromagnetic wave description of light and can therefore compute the amplitude, phase and polarization of the optical field at any position in the system. It can also account for common light delivery and detection components such as lenses, optical fibres and photo-detectors, allowing practical systems to be simulated. The model was validated against wavelength resolved measurements of transmittance and reflectance obtained using a system consisting of an FP etalon illuminated by a focussed Gaussian beam. Experiments with focal spot sizes ranging from 30 µm to 250 µm and FP etalon mirror reflectivities in the range 97.2 % to 99.2 % yielded excellent visual agreement between simulated and experimental data and an average error below 10% for a range of quantitative comparative metrics. We expect the model to be a useful tool for designing, understanding and optimising systems that use FP etalons.

1. Introduction

Fabry-Pérot (FP) etalons [1] consist of an optical cavity formed between two parallel mirrors as shown in Fig. 1(a). FP etalons are used in various applications, for example as multiplexers in telecommunications [2], frequency combs in metrology [3], resonators in lasers [4], tunable filters in spectroscopy [5], and sensors in biomedical imaging [6]. The optical power reflected or transmitted by an FP etalon as a function of wavelength is known as its Interferometer Transfer Function (ITF), illustrative examples of which are shown in Fig. 1(b). The ITF is very sensitive to the ratio between the wavelength and the optical path length traversed by a plane wave making a round trip inside the cavity. When this optical path length matches an integer number of wavelengths, light inside the cavity is said to be in resonance and the wavelength is referred to as the resonant wavelength. Close to the resonant wavelength, a small change in wavelength can give rise to a rapid change in transmitted and reflected powers, creating a so-called interferometric fringe. A highly reflective FP etalon illuminated by a collimated beam produces narrow fringes, making the device a highly effective spectral filter. Furthermore, since the resonant wavelength is highly sensitive to changes in the cavity's optical thickness, FP etalons can also be used for sensing [7]. For example, FP etalons can be used to detect pressure and temperature changes that modify the cavity optical thickness and, in turn, the reflected and transmitted power.

#382526 https://doi.org/10.1364/OE.382526
Journal © 2020 Received 6 Nov 2019; accepted 12 Jan 2020; published 28 Feb 2020

Optics EXPRESS

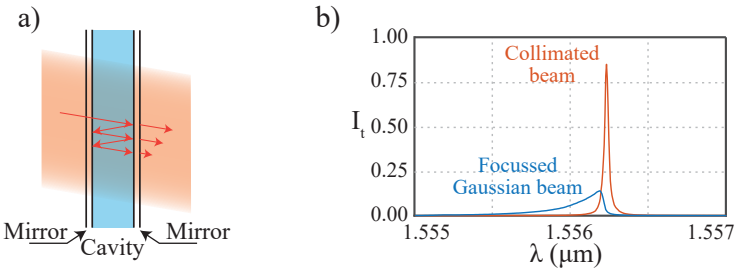

Fig. 1. a) Schematic diagram of a collimated beam transmitted through an FP etalon; b) ITFs acquired for collimated and focussed Gaussian beams.

When FP etalons are illuminated by a collimated beam, the ITF is accurately predicted by the Airy function [8]. However, in many systems, FP etalons are illuminated by more complex beams such as focussed Gaussian beams. Examples of such systems include External Fibre Fabry-Pérot Interferometer (EFPI)s [9,10], angular selective filters [11–13] and planar FP sensors for the detection of ultrasound [14–16]. An FP etalon illuminated by a focussed Gaussian beam, as opposed to a collimated beam, exhibits an ITF with fringes that are typically broader, more asymmetric and of lower visibility (metric of the fringe height), as shown in Fig. 1(b). In these circumstances the Airy function is no longer valid and a more sophisticated model is needed to replicate experimental results.

Previous studies have modelled FP etalons illuminated by non-collimated beams. For example, Abu-Safia *et al.* [17] applied a Gaussian beam propagation method to calculate the transmitted beam after each round trip of the FP etalon cavity and summed these to provide the total transmitted field. This technique, referred to as the unfolded cavity approach [18], was used to study the effect of the angle of incidence of the beam upon the ITF. This method is limited by being applicable only to unaberrated Gaussian beams and by the computational burden due to each round trip being calculated independently. A different model of Gaussian beam propagation in FP etalons was reported by La Penna *et al.* [19]. This model treated the FP etalon as a waveguide by using a modal description of the light inside it. The model was used to study the impact of Gaussian beam focal spot size and cavity thickness upon the ITF. However, as with Abu-Safia *et al.* [17] , it is only applicable to unaberrated Gaussian beams.

Other previously developed models are applicable to arbitrary beams. For instance, Nichelatti *et al.* [20] and Lee *et al.* [21] modelled beam propagation inside an FP etalon using the angular spectrum formalism [22]. Arbitrary incident beams were represented as a superposition of plane waves and the interaction of each with the FP etalon was calculated using the appropriate Airy function. Nichelatti *et al.* [20] investigated changes in the fringe shape in response to variations in the Gaussian spot size and beam alignment. In Lee *et al.* [21], the optical response of the FP etalon is explained as a spatiospectral filter, allowing the relationship of fringe shape to Gaussian spot size, beam alignment and mirror alignment to be explained. The use of the angular spectrum formalism has the advantages of allowing the simulation of arbitrary beams, as well as being computationally efficient since the use of the Airy function obviates the need to calculate each round trip individually.

Previous models have predicted the assymetric shape of the fringe, the broading and the reduction in the visibility but none have been quantitatively validated with experimental data. For this purpose, a more rigorous model which makes fewer assumptions than previous models, as well as being capable of representing the principal experimental parameters of a practical optical system, is required. For example, they neglected phase changes that can occur upon reflection and transmission by the mirrors. This factor is particularly important when considering metallic mirrors and dielectric mirrors operated far from their design wavelengths. Also, in

Optics EXPRESS

previous models, the mirror response is assumed to be independent of the direction of the plane wave incident, which is not in general true, particularly for thick mirrors. Furthermore, existing models considered the propagation of unaberrated Gaussian beams, thus neglecting the impact of non-ideal optical components. In particular, lenses used to focus the light into the FP etalon typically aberrate the beam, thus impacting the optical response of the FP etalon. Finally, in previous models, the light detector is assumed to be infinite in extent which precludes the modelling of commonly used detection methods in which the light is delivered to the photodetector via an optical fibre or pinhole.

In this paper, we present a model that solves Maxwell's equations for arbitrary plane waves incident upon an FP etalon which is represented by its physical structure, i.e., the refractive index and thickness of every layer of the structure including the cavity. We then couple this theory with an electromagnetic description of light focussing in a manner similar to van de Nes *et al.* [23]. We have, however, extended van de Nes *et al.*'s model to calculate the signal measured using a range of detection schemes such as optical fibre-coupled detectors [24,25]. The resultant model is versatile and able to model a wide range of experimental factors such as arbitrary beams, aberrations, detection schemes and FP etalons described by their physical structure as opposed to their mirror reflectivities and cavity. To test the model, we built and characterized an experimental setup that allowed us to illuminate an FP etalon with a focussed Gaussian beam and measure the reflected and transmitted intensity. We then qualitatively and quantitatively compared experimental and modelled ITFs to validate our model.

2. Model

We have developed a theoretical model to predict the fields transmitted and reflected by an FP etalon when it is illuminated with a focussed beam. This enables the ITF to be calculated. As illustrated in Fig. 2, the model decomposes the optical readout of an FP etalon into three main components: the illumination optics, which focus the illumination light onto the FP etalon, the FP etalon itself and the detection optics, which convert the light into a measurable signal. Each of those components are considered in detail in the Secs. 2.1, 2.2 and 2.3, respectively.

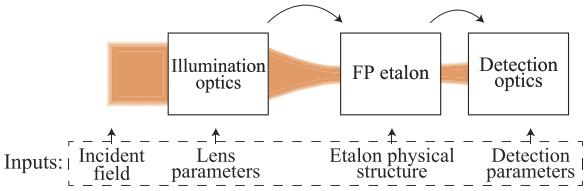

Fig. 2. Schematic diagram of the general optical system modelled.

2.1. Illumination optics

This part of the model describes the propagation in free-space of the focussed beam that is incident on the FP etalon to be calculated. In general, the illumination optics can be represented by a single lens which focusses a collimated beam onto the FP etalon. Therefore, the principal input of this section is the field incident on the back focal plane of the lens and the output is the field in the focal region of the lens. Fig. 3 illustrates the notation used when describing the focusing of light by a lens, denoted the objective. The field in the focal plane can be described as an angular spectrum of plane waves, i.e., as a sum of plane waves with complex amplitude $\hat{\mathbf{E}}_{\mathbf{in}}$ each propagating with direction $(\theta_{\text{in}}, \phi_{\text{in}})$ [26]. The complex amplitude, $\hat{\mathbf{E}}_{\mathbf{in}}$, of the plane wave propagating with direction $(\theta_{\text{in}}, \phi_{\text{in}})$ is only dependent on the field $\mathbf{E_b}$ at the point (x_b, y_b) in the

Optics EXPRESS

back focal plane according to [22]:

$$\begin{aligned}\hat{\mathbf{E}}_{\mathbf{in}}(\theta_{in},\phi_{in}) = t(\theta_{in})\,(\mathbf{E_b}(x_b,y_b)\cdot\mathbf{n}_\rho(x_b,y_b))\,(-\mathbf{n}_\theta(\theta_{in},\phi_{in}))\cos\theta_{in}^{-\frac{1}{2}}\\ + t(\theta_{in})\,(\mathbf{E_b}(x_b,y_b)\cdot(-\mathbf{n}_\phi(x_b,y_b)))\,\mathbf{n}_\phi(\theta_{in},\phi_{in})\cos\theta_{in}^{-\frac{1}{2}},\end{aligned} \tag{1}$$

where $(x_b,\ y_b)$ are the coordinates in the back focal plane related to the plane wave direction of propagation by:

$$(x_b,\ y_b) = (-f\sin\theta_{in}\cos\phi_{in}, -f\sin\theta_{in}\sin\phi_{in}), \tag{2}$$

where f is the lens focal length and t is the lens transmissivity which, for ideal lenses, is defined by the lens Numerical Aperture (NA) as:

$$t = \begin{cases}1, \text{ if } \theta_{in} \le \text{ asin NA}\\ 0, \text{ if } \theta_{in} > \text{asin NA}\end{cases}, \tag{3}$$

and $\mathbf{n}_{\boldsymbol{\rho}}$ and $\mathbf{n}_{\boldsymbol{\phi}}$ are the cylindrical coordinate system basis vectors and $\mathbf{n}_{\boldsymbol{\theta}}$ and $\mathbf{n}_{\boldsymbol{\phi}}$ are the spherical coordinate system basis vectors.

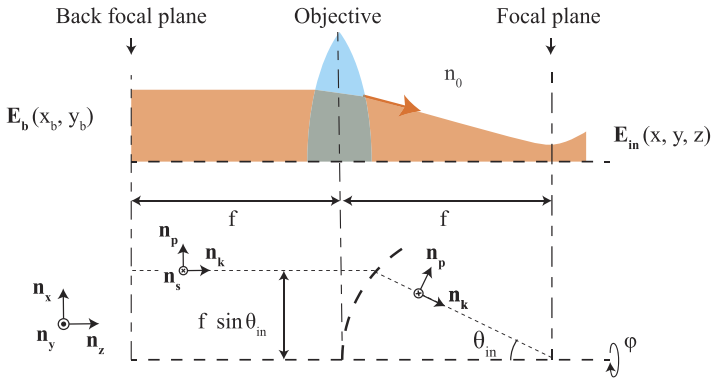

Fig. 3. Notation used to describe the light focusing by a lens, including the directions of light polarization and propagation. ($\mathbf{n_p}$, $\mathbf{n_s}$ and $\mathbf{n_k}$).

The field in the vicinity of the lens focus is then given by the coherent sum of all plane waves as [27,28]:

$$\begin{aligned}\mathbf{E}_{\mathbf{in}}(x,y,z) = k^2\int_0^{\pi/2}\int_0^{2\pi}\hat{\mathbf{E}}_{\mathbf{in}}(\theta_{in},\phi_{in})e^{in_0k\sin\theta_{in}(\cos\phi_{in}x+\sin\phi_{in}y)}\\ e^{in_0k\cos\theta_{in}z}\cos\theta_{in}\sin\theta_{in}\,d\phi_{in}\,d\theta_{in},\end{aligned} \tag{4}$$

where k is the wavenumber in vaccum $(2\pi/\lambda)$, λ is the wavelength in vaccum and (x,y,z) are the spatial coordinates relative to the lens focal point.

2.2. Fabry-Pérot etalon

An FP etalon is formed by a cavity between two mirrors which are typically created using a stack of dielectric thin films. Therefore, to model light propagation in the FP etalon, a multilayer structure is considered, i.e., a succession of A-1 parallel layers, each with refractive index N_i and thickness h_i, as shown in Fig. 4. A solution to Maxwell's equations exists for this geometry for plane waves with an arbitrary angle of incidence. This allows the solution for focussed incident beams to be obtained by using the angular spectrum form of the focussed beam.

Optics EXPRESS

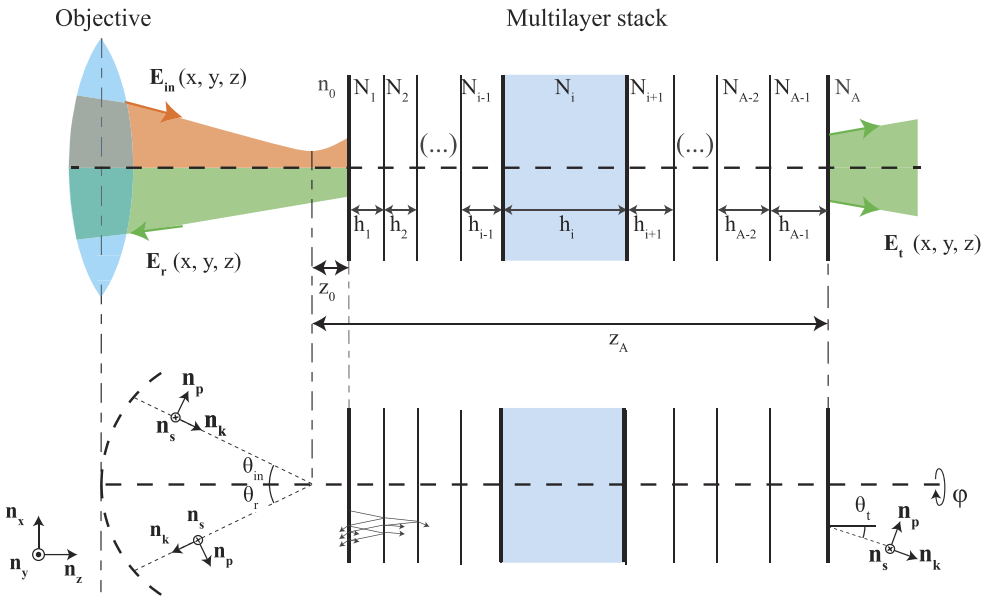

Fig. 4. Diagram illustrating the notation used to calculate how a focussed beam interacts with an FP etalon.

2.2.1. Transmitted and reflected plane wave.

The interaction between a plane wave and the FP etalon can be characterized by the reflection (${}^{p,s}r_{0\to A}$) and transmission (${}^{p,s}t_{0\to A}$) coefficients, where ${}^{p}r_{0\to A}$ is the ratio between the reflected and incident p polarized plane waves with incident direction θ_{in} to the FP etalon surface normal. The same rationale applies for the s polarized waves and for the transmission coefficients (if no superscript is used it refers to both the s and p polarizations). The coefficients $r_{0\to A}$ and $t_{0\to A}$ can be evaluated using the well established theory of optical interference in thin films [29]. This theory is based on consideration of the Fresnel reflection and transmission at each interface, along with the plane wave propagation between interfaces. The reflection and transmission coefficients are calculated by summing all the partially reflected and transmitted plane wave components which propagate away from the multilayer structure in the negative and positive z directions, respectively, and are given as:

$$r_{i\to A}(\theta_i) = \frac{r_{i\to i+1}(\theta_i) + r_{i+1\to A}(\theta_{i+1})\, e^{i2\beta_{i+1}}}{1 + r_{i\to i+1}(\theta_i)\, r_{i+1\to A}(\theta_{i+1})\, e^{i2\beta_{i+1}}}, \tag{5}$$

$$t_{i\to A}(\theta_i) = \frac{t_{i\to i+1}(\theta_i)\, t_{i+1\to A}(\theta_{i+1})\, e^{i\beta_{i+1}}}{1 + r_{i\to i+1}(\theta_i)\, r_{i+1\to A}(\theta_{i+1})\, e^{i2\beta_{i+1}}}, \tag{6}$$

where:

$$\beta_i = k h_i N_i \cos\theta_i, \tag{7}$$

$$\theta_i = asin\left(\frac{n_0}{N_i}\sin\theta_{in}\right), \tag{8}$$

$t_{i\to i+1}$ and $r_{i\to i+1}$ are the Fresnel transmission and reflection coefficients, respectively, for a plane wave incident on the interface between layers i and i+1, θ_i is the direction of propagation of the plane wave in the i$^{\text{th}}$ layer and is related with the propagation direction of the plane wave incident upon the FP etalon by Snell's law (Eq. (8)). β_i is the change in the plane wave phase due to the propagation in the i$^{\text{th}}$ layer. To calculate $r_{0\to A}$ and $t_{0\to A}$ for both polarization components, Eqs. (5) and (6) must be evaluated recursively from the A$^{\text{th}}$ to 1$^{\text{st}}$ layer of the FP etalon.

Optics EXPRESS

2.2.2. Transmitted and reflected angular spectrum.

The result of the previous section is now extended to all plane wave components of the illumination beam ($\hat{\mathbf{E}}_{\mathbf{in}}$). This is achieved by calculating the p and s polarized component of each plane wave component and applying the respective reflection or transmission coefficient. The polarized component can be found by mapping the field onto the basis vectors $\mathbf{n_s}$ and $\mathbf{n_p}$ which can be expressed in terms of the spherical coordinates basis vectors $\mathbf{n}_{\boldsymbol{\phi}}$ and $\mathbf{n}_{\boldsymbol{\theta}}$, respectively (see Fig. 4). Based on this approach, the reflected ($\hat{\mathbf{E}}_{\mathbf{r}}$) and transmitted ($\hat{\mathbf{E}}_{\mathbf{t}}$) angular spectrum are calculated according to [27]:

$$\begin{aligned}\hat{\mathbf{E}}_{\mathbf{r}}(\theta_r,\phi_r) = &(\hat{\mathbf{E}}_{\mathbf{in}}(\theta_{in},\phi_{in}) \cdot (-\mathbf{n}_{\theta}(\theta_{in},\phi_{in}))) \, {}^{p}r_{0\to A}(\theta_{in}) \, (-\mathbf{n}_{\theta}(\theta_r,\phi_r)) \, e^{ikn_0z_0(\cos\theta_{in}+\cos\theta_r)} \\ &+ (\hat{\mathbf{E}}_{\mathbf{in}}(\theta_{in},\phi_{in}) \cdot \mathbf{n}_{\phi}(\theta_{in},\phi_{in})) \, {}^{s}r_{0\to A}(\theta_{in}) \, (-\mathbf{n}_{\phi}(\theta_r,\phi_r)) \, e^{ikn_0z_0(\cos\theta_{in}+\cos\theta_r)},\end{aligned} \tag{9}$$

$$\begin{aligned}\hat{\mathbf{E}}_{\mathbf{t}}(\theta_t,\phi_t) = &(\hat{\mathbf{E}}_{\mathbf{in}}(\theta_{in},\phi_{in}) \cdot (-\mathbf{n}_{\theta}(\theta_{in},\phi_{in}))) \, {}^{p}t_{0\to A}(\theta_{in}) \, (-\mathbf{n}_{\theta}(\theta_t,\phi_t)) \, e^{ik(n_0z_0\cos\theta_{in}-N_Az_A\cos\theta_t)} \\ &+ (\hat{\mathbf{E}}_{\mathbf{in}}(\theta_{in},\phi_{in}) \cdot \mathbf{n}_{\phi}(\theta_{in},\phi_{in})) \, {}^{s}t_{0\to A}(\theta_{in}) \, \mathbf{n}_{\phi}(\theta_t,\phi_t) \, e^{ik(n_0z_0\cos\theta_{in}-N_Az_A\cos\theta_t)},\end{aligned} \tag{10}$$

where θ_r, θ_t and $\phi_{t,r}$ describe the direction of propagation of the transmitted and reflected plane waves and are defined as:

$$\theta_r = \theta_{in}, \tag{11}$$

$$\phi_r = \pi - \phi_{in}, \tag{12}$$

$$\theta_t = asin\left(\frac{n_0}{N_A}\sin\theta_{in}\right), \tag{13}$$

$$\phi_t = \phi_{in}, \tag{14}$$

where z_0 and z_A are the coordinates along the z-axis of the first and last interface of the FP etalon, relatively, to the focal point, respectively (see Fig. 4).

2.3. Light detection

Previous sections calculate how a focussed beam is reflected or transmitted from an FP etalon. In order to faithfully reproduce the signal measured by a practical system the transmitted or reflected field must be converted into the respective intensity value. The intensity measured is dependent on the readout scheme considered. Two different readout schemes are explained in this manuscript: a detector infinite in lateral extent and a single mode fibre based readout scheme.

2.3.1. Detector infinite in lateral extent.

When the beam size at the detector is much smaller than the readout area, as in Fig. 5(a), the intensity can be calculated assuming a detector infinite in lateral extent. In this circumstances, the detected intensity is given as [24]:

$$I \propto k^2 \int_0^{\frac{\pi}{2}} \int_0^{2\pi} \left|\hat{\mathbf{E}}_{\mathbf{t,r}}(\theta_{t,r},\phi_{t,r})\right|^2 \cos\theta_{t,r} \sin\theta_{t,r} \, d\phi_{t,r} \, d\theta_{t,r}. \tag{15}$$

2.3.2. Single mode fibre readout scheme

In a readout scheme based on a single mode fibre, as illustrated in Fig. 5(b), light is coupled into the fiber where it propagates until encountering a detector. The signal measured by the detector

Optics EXPRESS

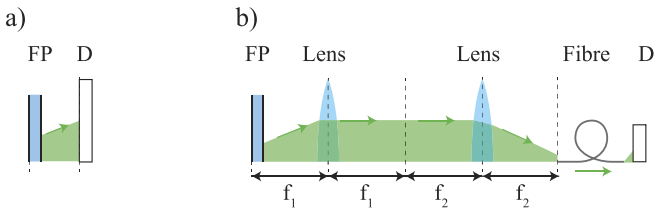

Fig. 5. Different detection schemes considered. a) and b) correspond to readout schemes based on a detector infinite in lateral extent and a single mode fibre, respectively. The abbreviations FP and D denote Fabry-Pérot etalon and Detector, respectively. $f_{1,2}$ is the focal length of the respective lens.

is given as [25]:

$$I \propto \left| \int_0^{\frac{\pi}{2}} \int_0^{2\pi} t_1(\theta_{t,r})\, t_2(\theta_{t,r})\, \Phi(\theta_{in}, \phi_{in})\, \hat{\mathbf{E}}_{\mathbf{t,r}}(\theta_{t,r}, \phi_{t,r}) \cos\theta_{t,r} \sin\theta_{t,r}\, d\phi_{t,r}\, d\theta_{t,r} \right|^2 \tag{16}$$

where Φ is the amplitude profile of the fibre mode, assumed to be Gaussian, given as:

$$\Phi = \exp\left(-\frac{f_1^2\, MFD^2\, k^2\, sin(\theta_{t,r})^2}{4 f_2^2} \right) \begin{bmatrix} 1 & 0 & 0 \\ 0 & 1 & 0 \\ 0 & 0 & 0 \end{bmatrix}, \tag{17}$$

where t_1 and t_2 are the lens transmissivities and *MFD* is the fibre Mode Field Diameter.

3. Experimental system and its characterization

The model was validated by comparing modelled and experimentally measured ITFs. The validation was performed in both transmission and reflection modes and for a range mirror reflectivities and illumination spot sizes. The experimental setup, illustrated in Fig. 6(a), was designed to measure both transmitted and reflected data simultaneously.

3.1. Experimental system

The illumination light, provided by a tunable cw laser (TSL 510, Santec), was coupled into to a circulator (6015-3 APC, Thorlabs) with MFD of (10.4±0.5) µm. Light is focussed onto the FP etalon surface by a combination of a collimator and an objective. Light reflected by the FP etalon propagates back through the collimator and the objective which couples the light back into the fibre. The circulator directs the reflected light to an InGaAs photodiode (G9801-22, Hamamatsu). Light transmitted through the FP etalon is detected using an InGaAs photodiode with active diameter of 2.0 mm (SM05PD5A, Thorlabs), with only free space (≃2 mm) between the FP etalon and the photodiode. In both readout schemes the active area of the detector was much larger than the incident optical field. Both photodiodes are connected to custom made transimpedance amplifiers [14] which are readout by a DAQ card (BNC-2110, National Instruments) connected to a computer. The illumation spot size was adjusted by using different combinations of collimator and objective, thus changing the optical system magnification. The lens combinations and the respective illumation spot sizes on the FP etalon are listed in Table 1.

In order to ensure that the spatial parameters of the beam incident upon the objective were accurately represented in the model, the beam emerging from the collimator was characterized using a beam profiler (Beam'R2, DataRay). The measured beam profile was used as an input

Optics EXPRESS

Table 1. Lenses used to achieve particular illumination spot sizes. $2\omega_0$ is the full width at $1/e^2$ of the Gaussian intensity profile. All lenses are produced by Thorlabs.

$2\omega_0$	Collimator	Objective
250 µm	TC12APC-1550 (f = 12.56 mm)	AC254-300-C (f = 300 mm)
85 µm	F280APC-1550 (f = 18.75 mm)	Pair of LA1301-C (f = 125 mm)
50 µm	F280APC-1550 (f = 18.75 mm)	Pair of LA1433-C (f = 75 mm)
30 µm	F280APC-1550 (f = 18.75 mm)	AC254-050-C (f = 50 mm)

to the model, in particular, to specify the profile of the beam incident on the objective's back focal plane. Since this setup employs low Numerical Aperture (NA) objectives, the impact of polarization is negligible and so, without loss of generality, the beam was assumed to be linearly polarized in the x-direction.

3.2. Fabry Pérot etalon

The FP etalon used has a fused silica cavity with thickness of 102 µm with custom made dielectric mirrors coated on both sides of the cavity (Fig. 6(b)). The mirrors were made by coating alternating layers of Zinc Sulfide (ZnS) and Sodium Hexafluoroaluminate (Na_3AlF_6) with a nominal optical thickness of $\lambda_{des}/4$ where λ_{des}, the design wavelength, was 1402 nm. This design was chosen so that the reflectivity is variable between 97.2 % and 99.2 % in the wavelength range of the tunable laser allowing us to validate the model for multiple mirror reflectivities with a single FP etalon.

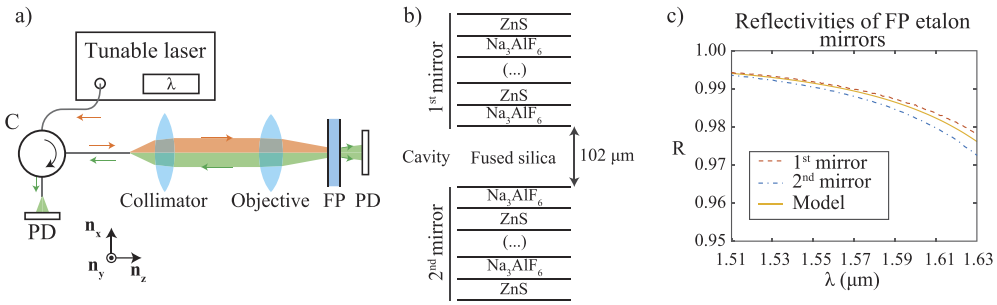

Fig. 6. a) Setup used to measure the FP etalon response in reflection and transmission. C, PD and FP denote Circulator, Photodiode and Fabry-Pérot etalon, respectively; b) Physical structure of the FP etalon; c) Measured and modelled reflectivity of the FP etalon mirrors. The modelled data is based on the design geometry of the mirrors, i.e., the thickness and refractive indices of the dielectric stack.

As part of the quality control process, during the coating of each of the FP etalon mirrors, a fused silica witness piece was coated at the same time. By measuring the reflectivities of the two witness pieces, the FP mirror reflectivities can therefore be estimated. The measured and simulated reflectivities of the two coatings are shown in Fig. 6(c). The measured reflectivity data was acquired by measuring the integrated intensity of a collimated beam reflected by each witness piece inclined at an angle of approximately 8° to the beam, as specified by the manufacturer. The modelled data was calculated using the model presented in this paper assuming an incident collimated beam at normal incidence. Ideally, the reflectivity of each mirror should be equal since they both have the same design geometry. However, the measured data shows a small discrepancy between the two reflectivities due, most likely, to fabrication imperfections, albeit

Optics EXPRESS

within the tolerance of the fabrication process. The simulated data corresponds to the mirrors' predicted reflectivity based upon the design geometry.

3.3. Calibration

The signal measured by both the transmission and reflection geometries in Fig. 6(a) depends of a number of factors including lens transmissivity, photodiode sensitivity, amplifier gain, fibre absorption and laser power. This dependence can be written as a wavelength dependent constant C. This allows the measured signal to be defined as the product of C and the underlying signal, I, as is predicted by the theoretical model as:

$$I_{raw}(\lambda) = I(\lambda)\, C(\lambda), \tag{18}$$

$I(\lambda)$ can be calculated by normalizing the measured signal I_{raw} by a reference measurement acquired using the same optical components under the same experimental conditions. However, different reference measurements are required for the transmission and reflection geometries as follows.

The reference response in reflection mode is the light measured assuming a perfect mirror, i.e., with reflectivity of 100 %, in the objective focal plane. For a wide spectral range, the position of the objective focal plane varies along the z-axis due to the chromatic aberrations as illustrated in Fig. 7(a). Thus, to acquire the reference measurement, the FP etalon in Fig. 6(a) was replaced by a dielectric mirror with known reflectivity, on a translation stage, to measure the reflected intensity as a function of the mirror axial position and wavelength. The data was then normalized by the wavelength dependent mirror reflectivity to calculate the signal that would be measured with a perfect mirror. The acquired data is illustrated in the graph of Fig. 7(b). At each sampled wavelength, the maximum intensity is assumed to be measured when the mirror is in the objective's focal plane. Therefore the reflection reference measurement is assumed to correspond to the maximum value of the data plotted Fig. 7(b), at each wavelength. The variations in the axial position at which the maximum intensity was achieved determines the variation in the focal length due to chromatic aberration. Both reflection reference measurements and variations in the focal length are displayed in Fig. 7(c).

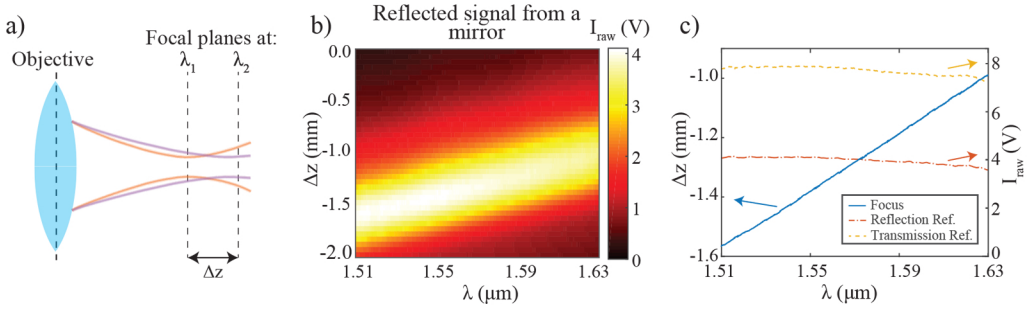

Fig. 7. a) Variations in the axial position of the objective focal plane due to chromatic aberrations; b) Reflected signal from a mirror as a function of the axial position and wavelength; c) Variations in the focal length as a function of wavelength along with the reference measurements for transmission and reflection. b) and c) were acquired using an illumination spot size $2\omega_0$ of 30 μm.

The transmission reference measurement used is the signal measured by the photodiode in transmission through the optical setup without an FP etalon in place. The photodiode active area was significantly larger than that of the transmitted beam so the measurement is unaffected by variations in the position of the objective focal plane [30]. For this reason, the transmission

Optics EXPRESS

reference measurement, plotted in Fig. 7(c), can be acquired by making a single intensity measurement at each sampled wavelength.

In order to compare the simulated and experimental data, both datasets were calibrated to the same units. The experimental data was calibrated as discussed in the previous paragraphs and the simulated data was calibrated in the same way by simulating the required reference measurements. This calibration step allows us to make absolute comparisons between simulated and experimental data. The procedure was repeated for all optical setups used to achieve different illumination spot sizes.

3.4. Alignment

In the experiments, the FP etalon was aligned at a given wavelength outside a fringe (in the baseline), which we denote as the alignment wavelength λ_f, by maximizing the reflected intensity using a tip-tilt stage and a translation stage along the optical axis. This step ensures that the first FP mirror is at the objective focal plane and that the FP etalon is normal to the objective's optical axis. However, due to the chromatic aberrations, the objective focal plane is only coincident with the first FP mirror at the alignment wavelength. The variation of the focal plane position (Δz) with wavelength was input into the model to calculate the relative distance between the FP etalon and the objective focal plane. The distance between the objective focal plane along the z-axis and the first FP etalon mirror is thus given as:

$$z_0(\lambda) = \Delta z(\lambda_f) - \Delta z(\lambda). \tag{19}$$

4. Results

A series of experiments were conducted to evaluate the performance of the model. Examples of transmitted and reflected ITFs, both experimental and simulated, with different illumination spot sizes $2\omega_0$ and alignment wavelengths λ_f are presented in Fig. 8. In general, there is a high level of agreement between the simulated and experimental data. The baseline variations were accurately predicted by the model, which exhibits its maximum at the alignment wavelength whilst reducing at wavelengths away from it, as predicted. The variation of the baseline depends on the chromatic aberration and illumination spot size. To achieve an illumination spot size of 30 µm an achromatic doublet was used for the objective. The lens is designed to minimize the chromatic aberrations, however, the impact on the experiment remains significant due to the wide spectral range considered.

In most practical applications, the shape of individual fringes is of utmost importance. To verify that the model faithfully reproduces individual fringes accurately, a collection of experimentally acquired and simulated ITFs are displayed in Fig. 9. The fringes are shown for different illumination spot sizes as well as mirror reflectivities. To make a fair comparison of the shape of the fringes acquired at different wavelengths, the impact of chromatic aberration was reduced by aligning the FP etalon axially such that it was in focus for a given alignment wavelength, which was chosen to be in a close vicinity of the fringe. The impact of chromatic aberrations can be neglected over the range of a fringe (<1 nm). The simulated data has been shifted along the wavelength axis (≃0.5 nm) to overlap the experimental data for comparison.

The plots in Fig. 9, show a very high level of agreement between the experimental and simulated data. The model accurately predicts the changes in the fringe shape as the mirror reflectivity, R, and the illumination spot size , $2\omega_0$, vary. To quantify the agreement, simulated and experimentally acquired fringe features have been compared. In particular, the visibility, Full Width Half Maximum (FWHM), Free Spectral Range (FSR) and the maximum absolute derivative, with respect to λ, of the ITF for wavelengths shorter (α) and longer (β) than the resonance wavelength are compared (see Fig. 10). The visibility and FWHM are metrics traditionally used to evaluate a fringe while α and β are relevant to FP sensors since they relate

Optics EXPRESS

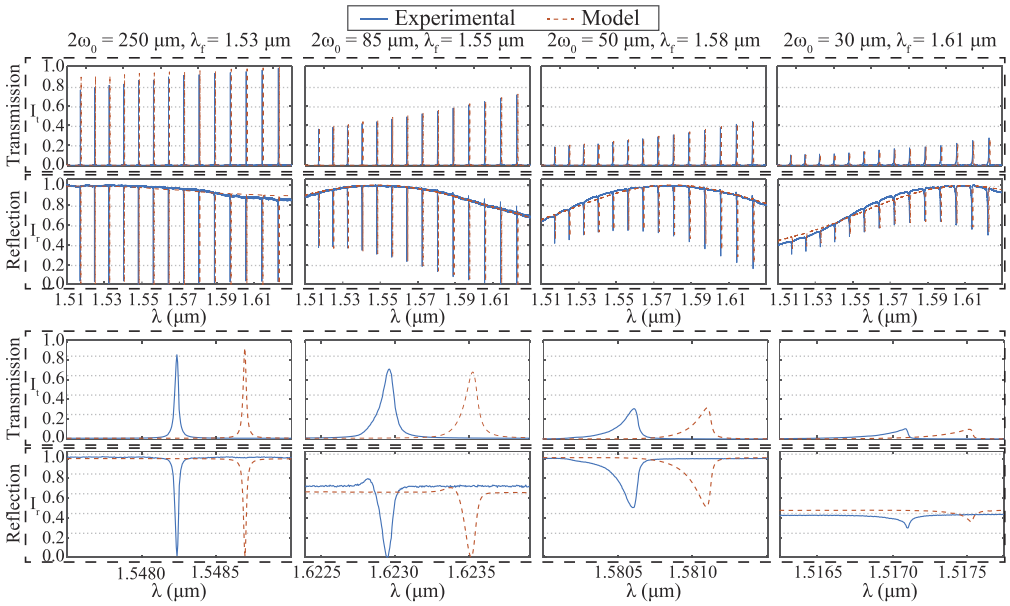

Fig. 8. Examples of transmitted and reflected ITFs obtained experimentally and simulated for a range of illumination focal spot sizes $2\omega_0$ and alignment wavelength λ_f. The bottom graphs are zoomed-in versions of the corresponding graph on top. All the data displayed is normalized by the respective reference response.

to sensitivity. The visibility for the transmission and reflection modes are defined as follows:

$$V_t = I_{max}, \tag{20}$$

$$V_r = \frac{I_{max} - I_{min}}{I_{max} + I_{min}}, \tag{21}$$

where I_{max} and I_{min} are the maximum and minimum intensity, respectively. The relative error ϵ between the simulated and experimental is defined for all metrics as

$$\epsilon = \frac{|\gamma_{exp} - \gamma_{mod}|}{\gamma_{mod}}, \tag{22}$$

where γ_{exp} and γ_{mod} are the respective metric considered (such as the visibility, FWHM, etc.) measured on the experimentally acquired and simulated fringe, respectively.

The visibility and the FWHM were computed for all fringes in all the ITF data sets. The values are plotted in Fig. 11 as a function of the average (of the first and second mirrors) mirror reflectivity. The results show that the model accurately predicts the trends observed experimentally due to the variations in the mirror reflectivity and the illumination spot size. The displayed error values are the average of the error between the experimental and simulated feature for all points of the respective graph. The model thus predicts both visibility and FWHM with an average error below 7 % for the range of illumination spot sizes and mirror reflectivities considered.

For the data set acquired with an illumination spot size of 85 μm, the small mismatch in the reflection mode visibility is due to the beam being apertured by the lens system, which leads to an increase in the visibility as observed. Another source of mismatch is the difference between the mirror properties assumed by the model and the actual mirror properties. As discussed in

Optics EXPRESS

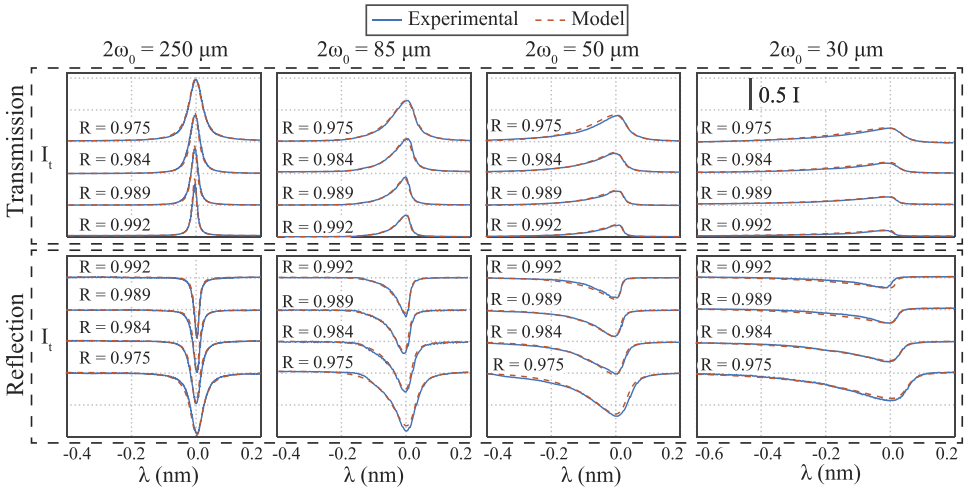

Fig. 9. Simulated and experimentally acquired fringes for $2\omega_0$ varying from 30 µm to 250 µm and R varying from 97.2 % to 99.2 %, for both transmission (top) and reflection (bottom) mode. The data is normalized by the corresponding reference response. The transmitted and reflected baselines correspond to 0 and 1, respectively. The scale bar in the right-top corner is valid for all graphs. The wavelength axis is centered on the resonance wavelength.

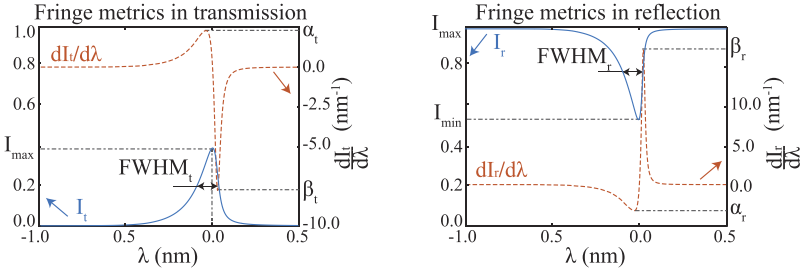

Fig. 10. Definition of the metrics used to characterized the fringe in both transmission and reflection mode.

Sec. 3.2, the reflectivities of the first and second mirrors were shown to differ slightly most likely due to limitations of the fabrication process. The model does not take these imperfections into account because it assumes that the mirrors match their manufacturer specifications.

Figure 12 shows plots of α and β values calculated from simulated and experimental data as a function of mirror reflectivity. It can be seen that as the illumination spot size decreases from 250 µm to 30 µm, the values of α reduce by up to two orders of magnitude, depending on the mirror reflectivity. A similar trend is observed in the value of β, which also reduces, albeit by only up to one order of magnitude. It can also be seen that, as the illumination spot size decreases, the values of α differ more from respective value of β due to the asymmetric shape of the fringe (as visible on Fig. 9). Both the trends and values observed in simulated and experimental α and β are in good agreement, with an average error ϵ of less than 10 %.

Up until this point, the model's accuracy has been quantified based on single fringes only. The wavelength spacing between successive fringes, i.e., the FSR, is also an important feature of the ITF. Therefore, to quantify the agreement in FSR, both experimentally acquired and simulated FSRs were computed and plotted on Fig. 13. Only the data set acquired in transmission mode

Optics EXPRESS

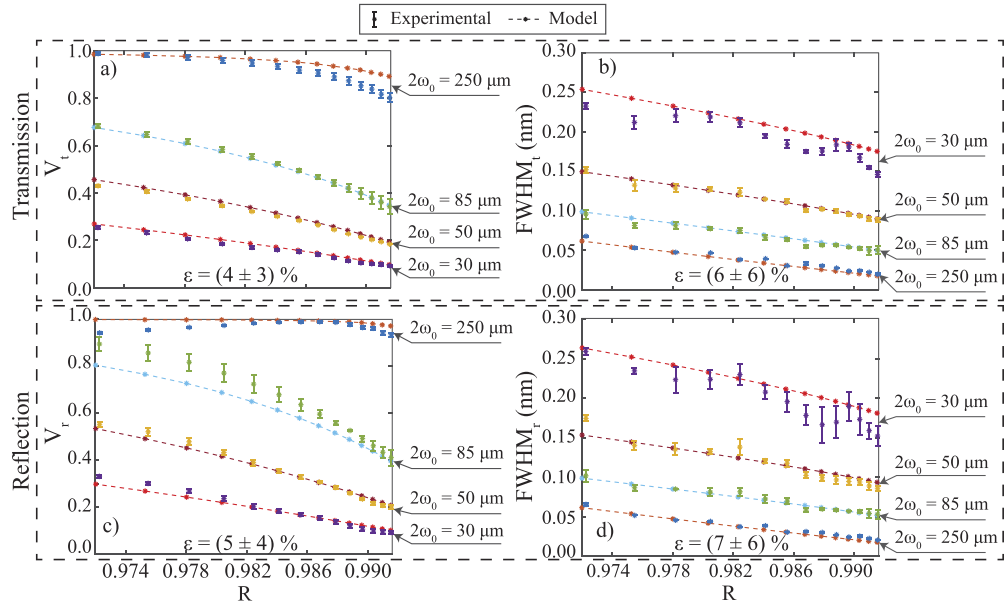

Fig. 11. Visibility and FWHM computed from the fringes acquired in transmission (top) and reflection (bottom) mode as a function of the mirror reflectivity R for multiple illumination spot size $2\omega_0$. The error values displayed are the average error of the points presented in the respective graph.

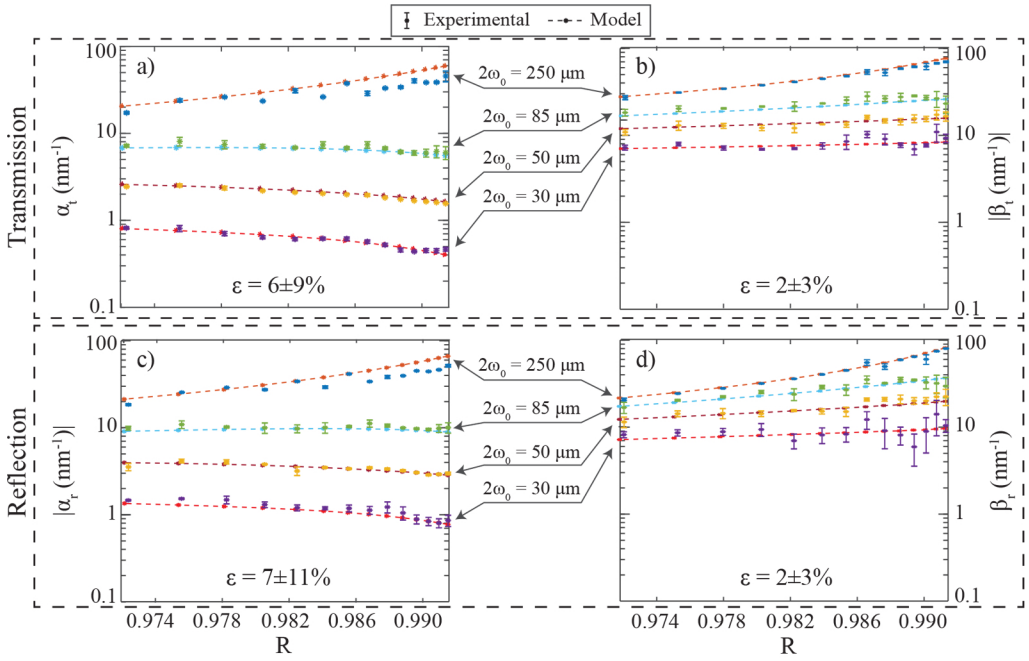

Fig. 12. Maximum absolute derivative at shorter (α) and longer (β) wavelength than the resonance wavelength (see Fig. 10) computed from the fringes acquired in transmission (top) and reflection (bottom) mode as a function of the mirror reflectivity R for multiple illumination spot size $2\omega_0$. The error values displayed are the average error of the points presented in the respective graph.

Optics EXPRESS

with an illumination spot size of 50 µm is displayed as it is representative of all data sets. The FSR calculated using the simulated and experimental data differs by only (0.1±0.1) %.

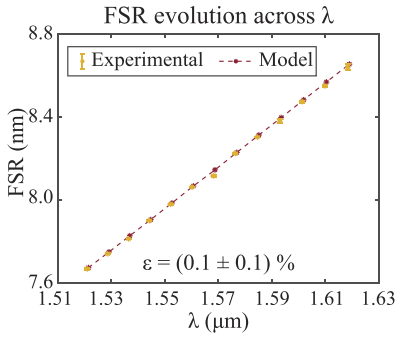

Fig. 13. Evolution of FSR across the spectral range from 1.51 µm to 1.63 µm for an illumination spot size $2\omega_0$ of 50 µm. The error value displayed is the average error of the points presented in the respective graph.

The model accurately replicated the experimentally acquired data for the range of experimental conditions considered. Therefore, the results from this section show the capacity of the model to accurately predict the optical response of an FP etalon illuminated with a focussed Gaussian beam in both transmission and reflection modes and for different readout schemes, mirror reflectivities and illumination spot sizes. The model is versatile and is applicable to more systems than are presented in this paper. We chose to validate the model for a high mirror reflectivity FP etalon because it is more challenging when compared to low mirror reflectivity due to the appearance of features such as the asymmetry in the fringe shape and visibility reduction. The model is also valid for other setups such as FP etalons with low mirror reflectivities, metallic mirrors or FP etalons illuminated by non Gaussian beams.

5. Conclusions

A full wave, vectorial, model of the interaction between a focussed beam and an FP etalon has been presented. The model takes into account a majority of practically relevant experimental parameters, including the illumination spot size, aberrations, mirror reflectivity and "detection" scheme. Furthermore, the model is applicable to both transmission and reflection modes. The model was validated by comparing simulated and experimental ITFs illuminated with a Gaussian beam varying from practically collimated ($2\omega_0$=250 µm) to focussed ($2\omega_0$=30 µm) and mirrors with reflectivities varying from 97.2 % to 99.2 %. In all conditions considered, the model accurately predicted the measured ITF achieving an average error below 10 % for all feature metrics considered. The results show that the model is capable of predicting the optical response of an FP etalon based solely on its design geometry and the characterization of the optical setup used.

The model presented in this work will find application in any field where an FP etalon is illuminated with focussed beam. For example, in the use of FP etalon as an angular selective filter, the model could be used not only to calculate the transmitted intensity, but also to study profile of the transmitted beam [31,32]. Another possible application is in the development of FP sensors illuminated with a focussed beam where the model might be useful for optimizing the sensitivity [33].

Optics EXPRESS

Appendix

Conventions

Throughout this paper, electromagnetic fields are assumed to be time harmonic and to follow the $e^{-i\omega t}$ time convention, which is omitted for brevity. The coordinate system denoted ($\mathbf{n_s}$, $\mathbf{n_p}$, $\mathbf{n_k}$) is used to describe the polarisation direction of fields in the model, where $\mathbf{n_s}$ and $\mathbf{n_p}$ refer to waves oscillating perpendicular and parallel, respectively, to the plane of incidence. $\mathbf{n_k}$ represents the propagation direction of light (Ch. 2 of ref. [29]).

Funding

Engineering and Physical Sciences Research Council (EP/L016478/1); European Research Council (741149); Royal Society (URF\R\191036, URF\R1\180435).

Disclosures

The authors do not declare any financial interests or conflicts of interest.

References

1. A. Perot and C. Fabry, "On the application of interference phenomena to the solution of various problems of spectroscopy and metrology," Astrophys. J. **9**, 87 (1899).
2. S. R. Mallinson, "Wavelength-selective filters for single-mode fiber WDM systems using Fabry-Perot interferometers," Appl. Opt. **26**(3), 430–436 (1987).
3. T. Steinmetz, T. Wilken, C. Araujo-Hauck, R. Holzwarth, T. W. Hänsch, and T. Udem, "Fabry-Pérot filter cavities for wide-spaced frequency combs with large spectral bandwidth," Appl. Phys. B **96**(2-3), 251–256 (2009).
4. Y. D. Jeong, Y. H. Won, S. O. Choi, and J. H. Yoon, "Tunable single-mode Fabry-Perot laser diode using a built-in external cavity and its modulation characteristics," Opt. Lett. **31**(17), 2586–2588 (2006).
5. P. D. Atherton, N. K. Reay, J. Ring, and T. R. Hicks, "Tunable Fabry-Perot Filters," Opt. Eng. **20**(6), 206806 (1981).
6. A. P. Jathoul, J. Laufer, O. Ogunlade, B. Treeby, B. Cox, E. Zhang, P. Johnson, A. R. Pizzey, B. Philip, T. Marafioti, M. F. Lythgoe, R. B. Pedley, M. a. Pule, and P. Beard, "Deep in vivo photoacoustic imaging of mammalian tissues using a tyrosinase-based genetic reporter," Nat. Photonics **9**(4), 239–246 (2015).
7. T. Yoshino, K. Kurosawa, K. Itoh, and T. Ose, "Fiber-optic Fabry-Perot interferometer and its sensor applications," IEEE J. Quantum Electron. **18**(10), 1624–1633 (1982).
8. M. Vaughan, *The Fabry-Perot interferometer: history, theory, practice and applications* (Routledge, 2017).
9. D. Rugar, H. J. Mamin, and P. Guethner, "Improved fiber-optic interferometer for atomic force microscopy," Appl. Phys. Lett. **55**(25), 2588–2590 (1989).
10. A. Oral, R. A. Grimble, H. Ö. Özer, and J. B. Pethica, "High-sensitivity noncontact atomic force microscope/scanning tunneling microscope (ne AFM/STM) operating at subangstrom oscillation amplitudes for atomic resolution imaging and force spectroscopy," Rev. Sci. Instrum. **74**(8), 3656–3663 (2003).
11. Z. L. Horvath, M. Erdelyi, G. Szabo, Z. Bor, F. K. Tittel, and J. R. Cavallaro, "Generation of nearly nondiffracting Bessel beams with a Fabry-Perot interferometer," J. Opt. Soc. Am. A **14**(11), 3009–3013 (1997).
12. A. Cox and D. Dibble, "Nondiffracting beam from a spatially filtered Fabry-Perot resonator," J. Opt. Soc. Am. A **9**(2), 282–286 (1992).
13. K. J. Koski, J. Müller, H. D. Hochheimer, and J. L. Yarger, "High pressure angle-dispersive Brillouin spectroscopy: A technique for determining acoustic velocities and attenuations in liquids and solids," Rev. Sci. Instrum. **73**(3), 1235–1241 (2002).
14. E. Zhang and P. Beard, "Broadband ultrasound field mapping system using a wavelength tuned, optically scanned focused laser beam to address a Fabry Perot polymer film sensor," IEEE Trans. Sonics Ultrason. **53**(7), 1330–1338 (2006).
15. Y. Hou, J.-S. Kim, S.-W. Huang, S. Ashkenazi, L. J. Guo, and M. O'Donnell, "Characterization of a broadband all-optical ultrasound transducer-from optical and acoustical properties to imaging," IEEE Trans. Sonics Ultrason. **55**(8), 1867–1877 (2008).
16. Y. Hou, Kim J.-s., S. Ashkenazi, L. J. Guo, and M. O'Donnell, "Broadband all-optical ultrasound transducers," Appl. Phys. Lett. **91**(7), 073507 (2007).
17. H. Abu-Safia, R. Al-Tahtamouni, I. Abu-Aljarayesh, and N. A. Yusuf, "Transmission of a Gaussian beam through a Fabry-Perot interferometer," Appl. Opt. **33**(18), 3805 (1994).
18. H. Varu, "The optical modelling and design of Fabry Perot Interferometer sensors for ultrasound detection," Ph.D. thesis, University College London (2014).
19. P. La Penna, A. Di Virgilio, M. Fiorentino, A. Porzio, and S. Solimeno, "Transmittivity profile of high finesse plane parallel Fabry-Perot cavities illuminated by Gaussian beams," Opt. Commun. **162**(4-6), 267–279 (1999).

Optics EXPRESS

20. E. Nichelatti and G. Salvetti, "Spatial and spectral response of a Fabry-Perot interferometer illuminated by a Gaussian beam," Appl. Opt. **34**(22), 4703 (1995).
21. J. Y. Lee, J. W. Hahn, and H.-W. Lee, "Spatiospectral transmission of a plane-mirror Fabry-Perot interferometer with nonuniform finite-size diffraction beam illuminations," J. Opt. Soc. Am. A **19**(5), 973 (2002).
22. L. Novotny and B. Hecht, *Principles of nano-optics* (Cambridge university press, 2012).
23. A. S. van de Nes, L. Billy, S. F. Pereira, and J. J. M. Braat, "Calculation of the vectorial field distribution in a stratified focal region of a high numerical aperture imaging system," Opt. Express **12**(7), 1281 (2004).
24. C. Sheppard and A. Choudhury, "Image Formation in the Scanning Microscope," Opt. Acta **24**(10), 1051–1073 (1977).
25. M. Gu, C. J. R. Sheppard, and X. Gan, "Image formation in a fiber-optical confocal scanning microscope," J. Opt. Soc. Am. A **8**(11), 1755 (1991).
26. M. R. Foreman and P. Török, "Computational methods in vectorial imaging," J. Mod. Opt. **58**(5-6), 339–364 (2011).
27. E. Wolf, "Electromagnetic diffraction in optical systems, II. Structure of the image field in an aplanatic system," Proc. Roy. Soc. A **253**(1274), 358–379 (1959).
28. B. Richards and E. Wolf, "Electromagnetic Diffraction in Optical Systems II. Structure of the Image Field in an Aplanatic System," Proc. Roy. Soc. A **253**(1274), 358–379 (1959).
29. H. Fujiwara, *Spectroscopic Ellipsometry: Principles and Applications* (John Wiley & Sons, Ltd, Chichester, UK, 2007).
30. T. Wilson and C. Sheppard, *Theory and practice of scanning optical microscopy*, vol. 180 (Academic Press, London 1984).
31. F. K. Tittel and J. R. Cavallaro, "Generation of diffraction-free beams for applications in optical microlithography," J. Vac. Sci. Technol., B: Microelectron. Process. Phenom. **15**(2), 287–292 (1997).
32. K. J. Koski and J. L. Yarger, "Brillouin imaging," Appl. Phys. Lett. **87**(6), 061903 (2005).
33. E. Zhang, J. Laufer, and P. Beard, "Backward-mode multiwavelength photoacoustic scanner using a planar Fabry-Perot polymer film ultrasound sensor for high-resolution three-dimensional imaging of biological tissues," Appl. Opt. **47**(4), 561 (2008).